Journal of Magnetism and Magnetic Materials 524 (2021) 167663

Contents lists available at ScienceDirect

Journal of Magnetism and Magnetic Materials

journal homepage: www.elsevier.com/locate/jmmm

Permeability and resistivity estimations of SMC material particles from eddy current simulations

J. Vesa *, P. Rasilo

Unit of Electrical Engineering, Tampere University, Tampere 33720 Finland

ARTICLE INFO

Keywords:
B-H curve
Geometry generation
Magnetic contact
Material identification
Soft magnetic composite
Voronoi tessellation

ABSTRACT

In this article, we estimate numerical values of a complex permeability and an electrical resistivity of soft magnetic composite (SMC) material particles. The estimations are carried out against a measured loss curve and a measured effective dynamical permeability curve. The SMC material is imitated using automatically generated geometries with control over the scalings of the geometries as well as the thicknesses of the electrical insulations between individual particles. The estimation procedure is repeated for a wide range of insulation thicknesses and scalings. Consistency with the measured effective dynamical permeability suggests the estimated relative permeability of the particles to be of the order of hundreds. An estimate of 250–500 is found. If the scalings of the geometries are chosen using a microscope image of the SMC material as a reference, the estimated resistivity of the particles is of the order of 10^{-7} Ωm.

1. Introduction

Soft magnetic composite (SMC) materials consist of ferromagnetic particles compressed and annealed. SMC materials have some advantages over laminated steels. SMCs usually have very fine particle-scale structures and thus they are applicable in wide frequency ranges. Isotropy of the material, observed in macroscale, may be imposed. Two well-written literature reviews of SMCs are referred to [1,2]. A microscope image of an SMC material is found in Fig. 1a.

In this article, we focus on estimating localized material parameters of an SMC material. Such parameters cannot be directly measured, but they play an important role in modeling of SMC materials. Particularly, we estimate the resistivity and the complex permeability of the magnetizing particles of a specific material, so that computations are in agreement with measurements of frequency-dependent losses and effective permeability.

In the literature, numerical values of conductivities in SMC materials seem to be reasonably consistent. Maruo et al. used 10^7 S/m [3]. In the computational articles of Ren et al., a conductivity of $1.12{\cdot}10^7$ S/m was used [4–6]. Bordianu and Bottauscio et al. used 10^7 S/m as well [7,8]. Permeabilities of SMC particles, however, have very large discrepancies in the literature. As pointed out by Sato et al., a direct measurement of such permeability is very difficult to obtain [9]. Ito and Maruo et al. used 100 as a relative permeability in the computations [3,10]. Vesa et al. used nonlinear relations with zero-field relative permeabilities of 270 and 420 [11]. Bordianu et al. used a relative permeability of 450 [7]. Ito and Waki et al. used relative permeabilities of 1000 [12,13]. In the articles of Ren et al. a relative permeability of 4000 was used [4–6]. The zero-field relative permeability in the article by Henneron et al. was close to 10 000 [14]. Vesa et al. showed that a wide range of relative permeabilities of SMC particles provide consistent results with a measurement of an effective permeability, provided that the thicknesses of the electrical insulations between the magnetizing particles have been chosen appropriately [15]. These discrepancies in the literature suggest that the localized properties of the models of SMC materials have not been properly understood.

In this article, we put forward evidence that for one specific SMC material, a relative permeability with magnitude of just a few hundred yields results more consistent with measurements compared to a model with the localized relative permeability of the order of several thousands. On the other hand, we show that the conductivity 10^7 S/m used in the literature is realistic.

2. Measurements

A Magnetics Inc. C055106A2 MPP was used as a test sample [16]. The toroid was wound and a two-coil setup was used, with the primary circuit consisting of the primary coil and a resistor in series. The primary circuit was fed with a sinusoidal voltage excitation. The primary current was measured by measuring the voltage over the resistor. The magnetic

* Corresponding author.

https://doi.org/10.1016/j.jmmm.2020.167663
Received 31 August 2020; Received in revised form 26 October 2020; Accepted 8 December 2020
Available online 25 December 2020
0304-8853/© 2020 The Author(s). Published by Elsevier B.V. This is an open access article under the CC BY license (http://creativecommons.org/licenses/by/4.0/).

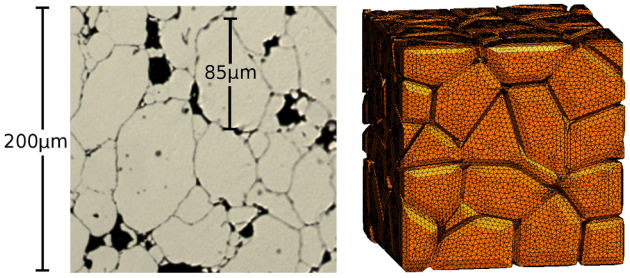

Fig. 1. (a) A microscope image of a Fe-Ni-Mo alloy SMC [11,16]. (b) A generated imitation of an SMC material geometry.

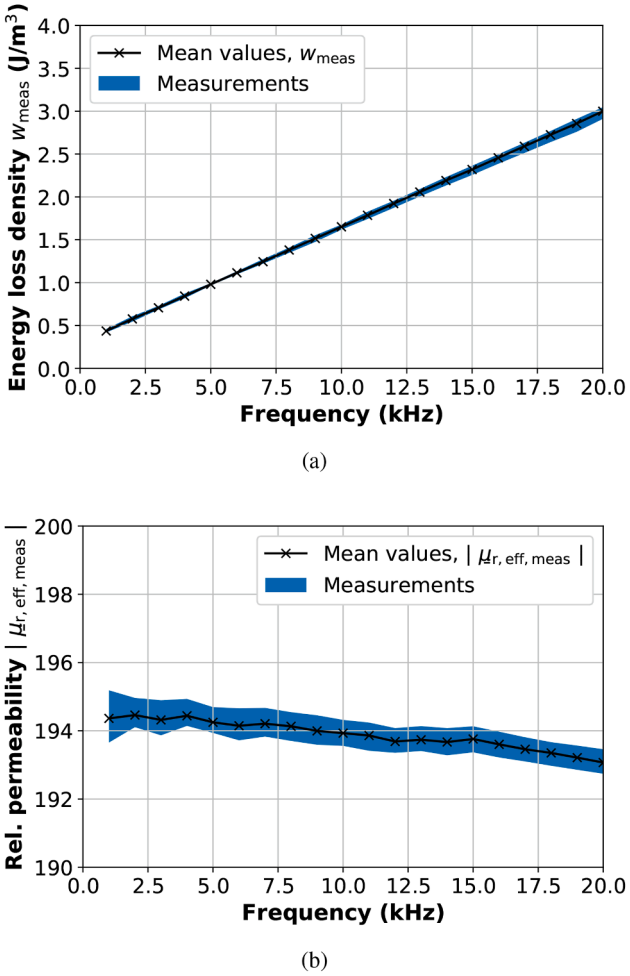

Fig. 2. Measurement data. (a) Measured energy loss density over one period of excitation. (b) Measured absolute effective permeability.

field strength H in the material was calculated from the primary current. The magnetic flux density B in the material was calculated from the integral of the secondary voltage. A frequency sweep up to 20 kHz was carried out. With each frequency, the peak value of the magnetic flux density was iterated to be 0.05 T.

One period of each signal was captured and energy loss densities of $w_{meas} := \int HdB$ over one period of excitation were computed. In Fig. 2a, there is a blue patch, inside which there are 20 measurement series. The black crosses indicate the mean values of each collection of losses. In this article, we refer to these mean values as 'measurement values'.

Sinusoidal curve fitting was done for the measured waveforms of B and H, and complex permeabilities, defined by the ratios of complex $\underline{B}$ and $\underline{H}$ phasors, were computed for each 20 measurements and each frequency. The magnitude of the complex relative permeability $\underline{\mu}_{r,eff,meas}$ has been visualized in Fig. 2b. Each 20 measurements are inside the blue patch, and the black crosses indicate the mean values of the measurements. In this article, we refer to these mean values as 'measurement values'.

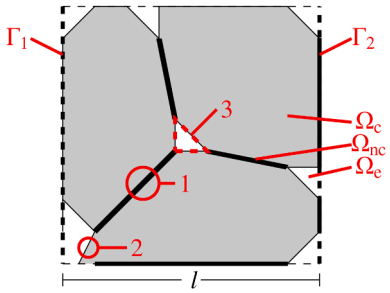

Fig. 3. A schematic of the geometries.

3. Methods

In this section, we discuss two matters. First, we consider the finite element model and the estimation problem used in finding material parameters for SMC particles. Second, we describe two sets of geometry imitations that are used in the computations.

3.1. Computational methods

Let us consider a geometry, for instance the right one shown in Fig. 1. It is much like the simplified schematic image appearing in Fig. 3. Denote the conductive particles with Ω_c and the non-conductive insulation layers, denoted by the thick black lines and the number 1 shown in Fig. 3, by Ω_{nc}. Furthermore, denote the thicker empty regions, visualized in Fig. 3, by Ω_e.

We assume that the permeability ratio between Ω_c and Ω_e is high. Hence, it makes sense to assume that $\mathbf{B}\cdot\mathbf{n} = 0$ holds on the surfaces between Ω_e and Ω_c. The surfaces are denoted by the number 2 in Fig. 3. Furthermore, we assume that the caves, indicated by the dashed boundary line and the number 3 in Fig. 3, admit no currents. Therefore the integrals of $\mathbf{H}$ along such boundary loops vanish. Finally, we assume that time derivatives of surface integrals of $\mathbf{B}$ over surfaces cutting the caves, denoted by the number 3 in Fig. 3, are insignificant. This is a consequence of the high permeability ratio between Ω_c and Ω_e. Thus, the changes in magnetic fluxes in the caves, denoted by the number 3 in Fig. 3, do not contribute to electromotive forces over loops around the caves. Due to these assumptions, we neglect the thick insulation regions Ω_e and solve the necessary fields in $\Omega = \Omega_c \cup \Omega_{nc}$.

The conductive regions Ω_c are meshed with tetrahedra. The non-conductive regions Ω_{nc} are meshed with degenerate prisms whose thicknesses may be adjusted freely [15]. Effectively, the degenerate prisms are just right-angled prisms whose Jacobians are modified in order to imitate a finite thickness. All the components of Ω_c and Ω_{nc} are simply connected. Hence, we use a tree-gauged $\mathbf{T}$-φ formulation on Ω. Let us denote the resistivity of the material particles by ρ and the complex relative permeability of the particles by $\underline{\mu}_r$ (complex-valued quantities underlined). The equations in Ω_c are given by

$$\nabla \times \left(\rho \nabla \times \underline{\mathbf{T}}\right) = -j\omega \underline{\mu}_r \mu_0 \left(\underline{\mathbf{T}} - \nabla \underline{\varphi}\right), \nabla \cdot \underline{\mu}_r \mu_0 \left(\underline{\mathbf{T}} - \nabla \underline{\varphi}\right) = 0. \quad (1)$$

The potential $\underline{\mathbf{T}}$ vanishes on $\partial\Omega_c$ and in Ω_{nc}. In Ω_{nc} it holds that

$$\nabla \cdot \left(\underline{\mu}_r \mu_0 \nabla \underline{\varphi}\right) = 0. \quad (2)$$

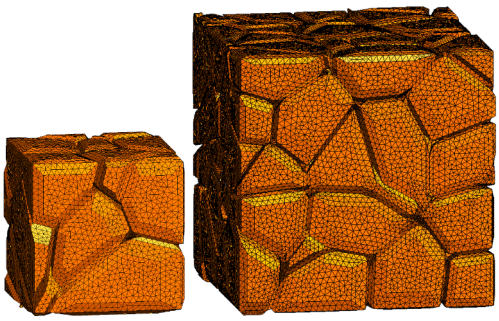

Fig. 4. Geometry (left) consists of 27 particles. There are approximately 30 000 nodes in 230 000 elements. Geometry (right) consists of 125 particles. There are approximately 140 000 nodes in 1 100 000 elements.

The potential $\underline{\mathbf{T}}$ is interpolated using an edge basis neglecting the spanning trees of each material particle in Ω_c. The potential $\underline{\varphi}$ is interpolated using a nodal basis. The equations are discretized by the Galerkin method.

Boundary conditions for $\underline{\varphi}$ are set on Γ_1 and Γ_2, depicted in Fig. 3. We set $\underline{\varphi} = 0$ on Γ_1 and $\underline{\varphi} = \underline{H}_{\text{eff}} l$, where $\underline{H}_{\text{eff}}$ represents an externally applied field and l is the total width of the material inclusion. This $\underline{H}_{\text{eff}}$ is chosen to be real. Furthermore, it is frequency-dependent and it is taken directly from the measurements. Effective $\underline{B}_{\text{eff}}$ may be computed by

$$\underline{B}_{\text{eff}} = \frac{1}{\text{Vol}} \int_{\Omega} \underline{\mathbf{B}} \cdot \mathbf{e}_1 , \tag{3}$$

where Vol stands for the total volume of the material inclusion and $\mathbf{e}_1$ is the basis vector perpendicular to Γ_1 and Γ_2. Effective complex relative permeability $\underline{\mu}_{\text{r,eff}}$ is defined as the ratio of $\underline{B}_{\text{eff}}$ and $\underline{H}_{\text{eff}}$ divided by the vacuum permeability.

In addition to dynamical permeabilities, we are interested in losses. From complex field solutions, eddy current loss densities may be computed by

$$w_{\text{ed}} = \text{Re}\left\{ \frac{1}{\text{Vol}} \frac{1}{f} \int_{\Omega_c} \frac{1}{2} \overline{\underline{\mathbf{J}}} \cdot \rho \underline{\mathbf{J}} \right\} \tag{4}$$

and hysteresis losses by

$$w_{\text{hy}} = \text{Re}\left\{ \frac{1}{\text{Vol}} \int_{\Omega_c} \overline{\underline{\mathbf{H}}} \cdot \pi j \underline{\mathbf{B}} \right\}. \tag{5}$$

The derivations of these formulas are similar to the one presented by Ren et al. [6].

The perspective in this article is inverse modeling. We know by measurements what to expect for losses and the dynamical effective permeability. The computational model takes two material parameters, a complex relative permeability $\underline{\mu}_{\text{r}}$ and a resistivity ρ as inputs, and computes losses $w = w_{\text{ec}} + w_{\text{hy}}$ and the effective complex relative permeability $\underline{\mu}_{\text{r,eff}}$. We define a squared error

$$e\left(\underline{\mu}_{\text{r}}, \rho\right) = \sum_{f \in F} \left[\left(\frac{w\left(f, \underline{\mu}_{\text{r}}, \rho\right) - w_{\text{meas}}\left(f\right)}{w_{\text{meas}}(f)} \right)^2 + \left(\left| \underline{\mu}_{\text{r,eff}}\left(f, \frac{\underline{\mu}_{\text{r}}, \rho\right)}{\left| \underline{\mu}_{\text{r,eff,meas}}\left(f\right) \right|} \right| - \left| \underline{\mu}_{\text{r,eff,meas}}\left(f\right) \right| \right)^2 \right], \tag{6}$$

where $F = \{5, 15\}$ kHz. We find suitable material parameters $\underline{\mu}_{\text{r}}$ and ρ by minimizing e using the dogbox algorithm implemented in the Scipy least squares package [17].

Table 1
Geometry template I.

N	$3^3 = 27$
d	0.45/3
w_{F}	[0,0.4]
w_{C}	[0.1,0]

Table 2
Geometry template II.

N	$5^3 = 125$
d	0.45/5
w_{F}	[0,0.4]
w_{C}	[0.1,0]

3.2. Geometry imitations

Following our previous articles, we generate imitations of the SMC material automatically [11,15]. For details about SMC geometry imitations, we refer to these works. Consider the left geometry shown in Fig. 4. The geometry has been generated based on the parameters given in Table 1.

In a nutshell, in the cube $[0, 1]^3$, total $N = 3^3 = 27$ points have been randomly selected under the restriction that each point is at least the distance $d = 0.45/3$ away from one another. A Voronoi tessellation is computed from these points. Each face of each cell of the tessellation has been refined, and the refined faces have been shrunk to form gaps and contacts between neighbouring particles, based on the numerical information given in the vectors w_{F} and w_{C}. Total 200 randomized geometries of such kind were generated, with each of them having a fraction of 90% of the volume filled with SMC particles. Furthermore, each particle initially has 36% of their surface area in contact with the neighbouring particles. However, we emphasize that even though there are contacts in the generated geometries, there are no galvanic contacts among the particles in any of the computational models of this article. Instead, the 'contact surfaces' are modeled as non-conducting regions discretized by degenerate prisms with finite thicknesses, as explained in 3.1, to imitate insulations.

Another set of 200 geometries was generated, based on the parameters given in Table 2. These geometries are similar to the former set but with each inclusion having 125 particles. One geometry is shown on the right-hand side of Fig. 4. These geometries have the same volume fill factor and contact surface area factor as the smaller geometries.

4. Results

Estimations of localized complex permeabilities and resistivities are carried out in the following two subsections. Every estimation is based on the minimization of (6), and every time an estimation is carried out, both the complex permeability $\underline{\mu}_{\text{r}}$ and the resistivity ρ get numerical values.

In Section 4.1, we investigate how the estimated parameters depend on the thicknesses of the electrical insulation layers between the SMC material particles. We find that the estimated values of resistivity are

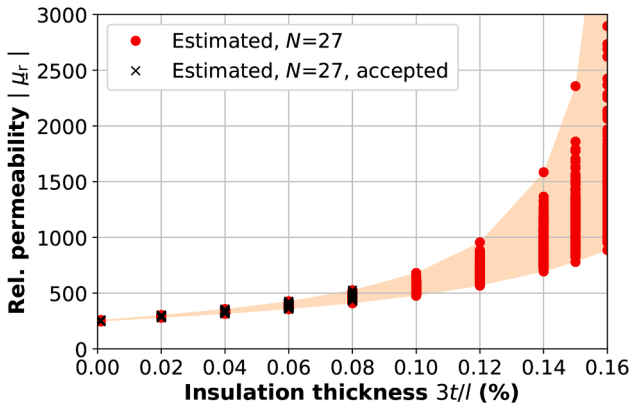

(a)

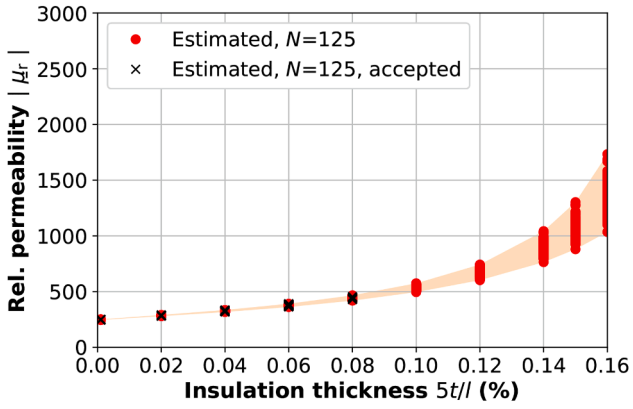

(b)

Fig. 5. Estimated absolute values of the localized permeability with respect to relative insulation thicknesses. (a) Estimations based on the 27-particle geometries. (b) Estimations based on the 125-particle geometries. The relative insulation thicknesses $3t/l$ and $5t/l$ have been explained in Section 4.1.

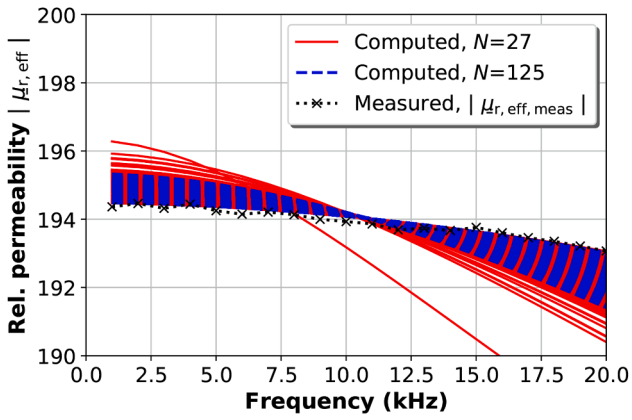

(a)

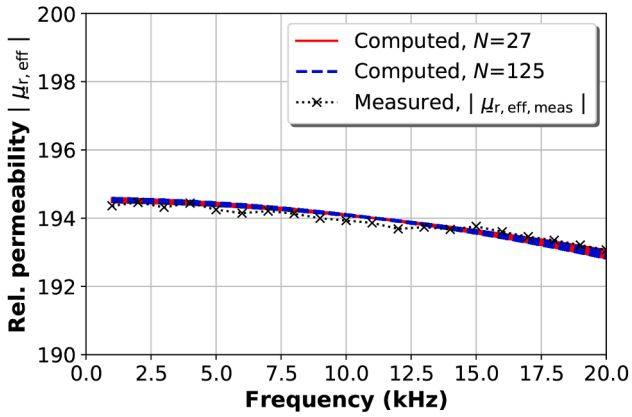

(b)

Fig. 6. Forward computations of effective absolute permeabilities. The simulations are based on the material parameters depicted in Figs 5, 11 and 12 and the corresponding geometries. (a) Computed effective absolute permeabilities for both sets of 200 geometries and ten insulation thicknesses. (b) This visualization includes only such curves from the plot ((a)) that obey the condition $e_2 < 0.8$.

reasonably independent of the insulation thicknesses but the permeabilities yield a clear dependence. To decide what is a realistic range of insulation thicknesses, and thus permeabilities, we compare computational effective dynamical permeabilities to the measured curve 2b.

In Section 4.2, we investigate how the estimated parameters depend on the scaling of the geometry imitations. We find that the estimated values of complex permeability are independent of the scaling but the resistivities yield a clear dependence. We draw a realistic value of the scaling from the microscope image 1a, and this sets a constraint to the estimated resistivity.

4.1. Estimations with respect to insulation thicknesses

Consistently to the microscope image, shown in Fig. 1, we scaled the generated geometries such that the edges of the $3^3 = 27$-particle geometry inclusions were scaled to $l = 3{\cdot}85\ \mu\text{m} = 255\ \mu\text{m}$. Similarly, the edges of the $5^3 = 125$-particle geometry inclusions were scaled to $l = 5{\cdot}85\ \mu\text{m} = 425\ \mu\text{m}$. The scaling $85\,\mu$m was found by computing the Feret diameters and the areas of the particles of a relatively large microscope image, from which Fig. 1a was extracted. The volume of the particles was estimated by $A^{3/2}$, where A represents the area of one particle. The scaling of $85\,\mu$m was found by taking the expected value from a distribution that characterizes the estimated volumes of the particles with respect to the Feret diameters. Hence, $85\,\mu$m represents a 'mean diameter' of the actual material particles.

For both two sets of 200 geometries, 10 different insulation layer thicknesses were defined. Deviations in the insulation thicknesses were not considered. Instead, we assumed that each insulation is of the same thickness t (that varies from model to model). The insulation thicknesses were controlled by modifying the Jacobians of the degenerate prisms, described in Section 3.1. For each geometry and insulation thickness, the estimation problem, defined by the minimization of the error function (6), was solved.

In Fig. 5, the absolute values of the estimated relative permeabilities are visualized. The insulation thicknesses in the plots have been characterized such that for the $3^3 = 27$-particle geometries, instead of expressing just the absolute insulation thickness t, we use a relative quantity $3t/l$, where l is the scaling of the geometry inclusion. Similarly, for the $5^3 = 125$-particle geometries, the insulation thicknesses have been characterized by the relative quantity $5t/l$. This way the insulation thicknesses are comparable independently of how many particles there are in the inclusion and how the geometries are scaled.

In Fig. 5, there are red dots, called 'Estimated, $N = 27$' and 'Estimated, $N = 125$', indicating the estimated magnitudes of the relative permeability of the material particles. As expected, the absolute values of the relative permeabilities are consistent with the earlier static results [15]. The thicker the insulations are, the higher the estimated magnitudes of the permeabilities are. Deviations due to the randomization of the geometries increase as the insulations get thicker. Increasing the number of particles in the inclusion decreases the deviations. The rest of

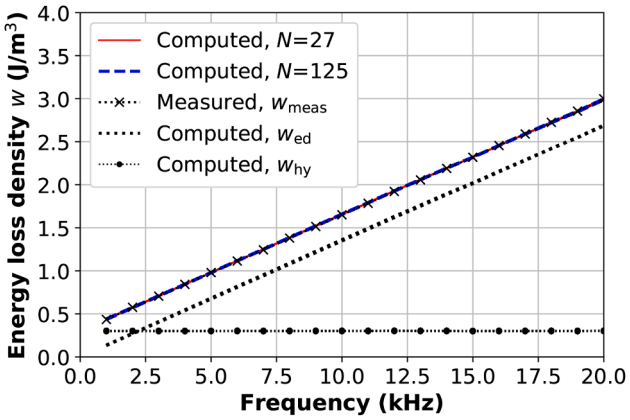

Fig. 7. Computed energy loss densities. The simulations are based on the material parameters depicted in Figs 5, 11 and 12 and the corresponding geometries. The plot contains all curves obtained using the geometries with relative insulation thicknesses less or equal to 0.08%.

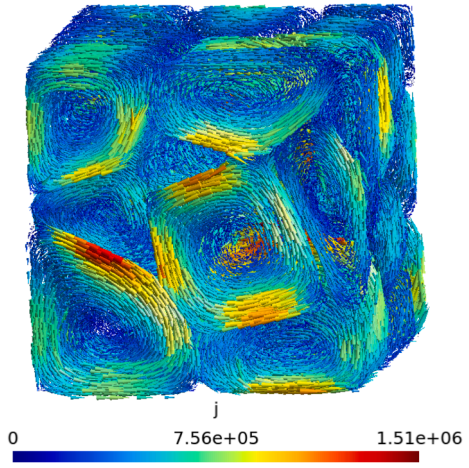

Fig. 8. A visualization of an eddy current field. A geometry with 27 particles is used. The edges of the cell are scaled to 3·85 μm = 255 μm. The insulations of the geometry are 0.02% thick, which corresponds to 17 nm absolute thickness. The relative permeability of the particles is approximately 300 with an angle of −0.01. The resistivity of the particles is approximately $1.3{\cdot}10^{-7}$ Ωm. The field is a mid-cycle still capture of a 10-kHz eddy current field.

the estimated parameters, namely the angle of the permeability and the electrical resistivity, play a lesser role in the considerations of this section. Hence, these results are presented in Appendix A. However, we note that the estimated resistivities, depicted in Fig. 12, are reasonably independent of the thicknesses of the electrical insulation layers.

In order to assess if some insulation thicknesses should be preferred over the others, we consider forward simulations. Both sets of 200 geometries with 10 insulation thicknesses and the corresponding estimated material parameters were used to compute the dynamical permeabilities, depicted in Fig. 6a. We see that some curves agree with the measurements better than the others. Let us filter the curves, depicted in Fig. 6a using an error function

$$e_2 = \left(\sum_{f=1,\dots,20\text{kHz}} \left| \left| \underline{\mu}_{\text{r,eff,meas}}\left(f\right) \right| - \left| \underline{\mu}_{\text{r,eff}}\left(f\right) \right| \right|^2 \right)^{\frac{1}{2}}. \tag{7}$$

Fig. 6b contains only such curves that admit an agreement with the measured curve under the condition $e_2 < 0.8$. In Fig. 5, the 'accepted' parameters that have been denoted by the black crosses over the red dots correspond to the same filtering by $e_2 < 0.8$ as in Fig. 6b. We see that a good agreement, defined by the criterion $e_2 < 0.8$ between the measured

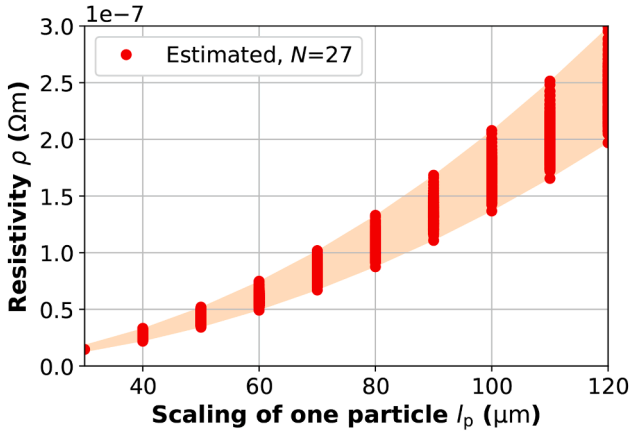

(a)

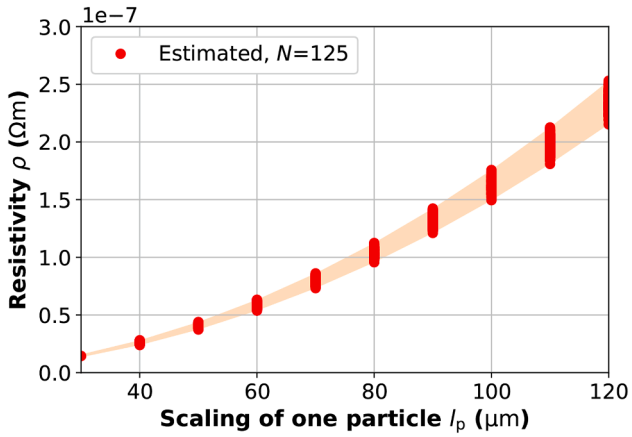

(b)

Fig. 9. Estimated resistivities with respect to the scaling of the material particles. (a) Estimations based on the 27-particle geometries. (b) Estimations based on the 125-particle geometries.

and computed dynamical effective permeabilities, correlates with low insulation thicknesses and low localized relative permeabilities in the model. This is due to skin effect becoming more and more dominant if the permeability of the particles is increased, thus making the frequency-dependent effective permeability curve more steep. If the models with $e_2 < 0.8$ are considered to be 'acceptable', we would say that the relative permeabilities of the material particles should be of the order 250–500. Similarly, the relative insulation thicknesses should be less than 0.08%. This corresponds to an absolute thickness of no more than 68 nn. To demonstrate that the models with insulation thicknesses lower than 0.08% admit a good agreement with the loss measurements, Fig. 7 depicts the measured and the computed losses. Fig. 7 also contains the computed eddy current- and hysteresis losses according to (4) and (5). The eddy current- and hysteresis loss curves contain both the results with the geometries of 27 particles, as well as the results with the geometries of 125 particles, with insulation thicknesses less or equal to 0.08%.

In Fig. 8, we see a visualization of an eddy current field. The field has been acquired using a 27-particle geometry in a 10-kHz simulation.

4.2. Estimations with respect to scalings of the geometries

Let us now change the perspective slightly. Let us choose a suitable relative insulation thickness and solve estimation problems with various scalings of the geometries. We use again the two sets of 200 geometries,

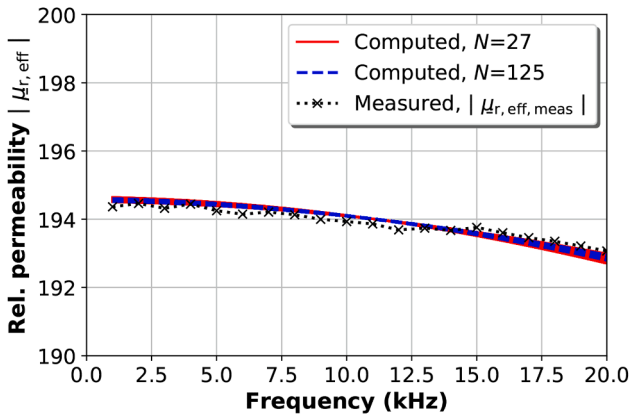

(a)

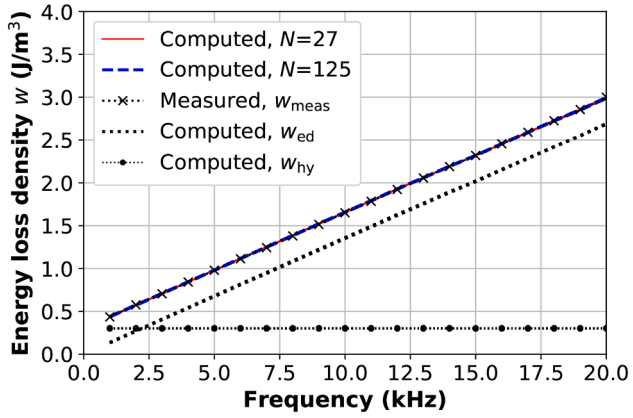

(b)

Fig. 10. Forward simulations based on the estimated material parameters, depicted in Figs. 9, 13 and 14. (a) Computed effective absolute permeabilities using both sets of 200 geometries and all 10 selected scalings of the particles with the corresponding estimated material parameters. (b) Computed energy loss densities over one period of excitation using both sets of 200 geometries and all 10 selected scalings of the particles with the corresponding estimated material parameters.

much like the geometries depicted in Fig. 4. We now fix the relative insulation thickness to 0.05%. We choose 10 scalings l_p, ranging from 30 μm to 120 μm, so that the edges of the $3^3 = 27$-particle geometry inclusions are scaled to $l = 3 \cdot l_p$ and the edges of the $5^3 = 125$-particle geometries are scaled to $l = 5 \cdot l_p$.

Estimations based on minimization of the error function (6) were carried out for both sets of 200 geometries, each with 10 different scalings. The estimated values of the localized resistivity of the particles are depicted in Fig. 9. In the visualizations, the resistivities have been plotted against the scaling l_p of one particle, and thus the results for the geometries with 27 particles are comparable with the results for the geometries with 125 particles. We see that the resistivity $10^{-7}\,\Omega$m corresponds to the scaling of the order of $80\,\mu$m. From the microscope image, depicted in Fig. 1a, we conclude that the reported values of the conductivity, of the order of 10^7 S/m, are realistic.

However, the estimated resistivity is not unique. If the scaling of the geometry is unknown or contains uncertainty, the estimated resistivity contains uncertainty as well. Uncertainty due to randomization of the geometries is also involved but comparing Figs. 9a and 9b, we conclude that increasing the number of particles in the inclusion decreases this uncertainty. The absolute values and the angles of the localized permeability were also estimated during the estimation procedures. These values play a lesser role in the considerations of this section, and thus the results are presented in Appendix B. However, we note that the estimated permeabilities, visualized in Figs 13 and 14, are independent of the scaling of the geometries.

To demonstrate that the estimated parameters yield realistic results in terms of energy losses and effective permeabilities, forward computations were carried out. Fig. 10 shows all forward model simulations for both sets of 200 geometries with all 10 scalings using the corresponding estimated material parameters. Additionally, 10b shows the computed eddy current- and hysteresis losses obtained by (4) and (5). These curves contain both the computations with the 27-particle geometries and the computations with the 125-particle geometries.

5. Concluding remarks

In this study, we used SMC geometry imitations and a time-harmonic model to compute losses and effective permeabilities of a specific SMC material. The model was used in order to estimate numerical values of localized material parameters, specifically a resistivity and a complex permeability, of the SMC material particles.

It was shown that in terms of computed effective dynamical permeabilities agreeing well with measurements, the magnitude of the localized relative permeability is of the order of hundreds. An estimate of 250–500 was found. The result is not unique in the sense that altering the electrical insulation thicknesses of the geometries and selecting the permeability accordingly, computations and measurements are in agreement. Localized relative permeabilities, used in the literature, range from 100 to several thousands [3,10,11,7,12,13,4–6,14,15]. This paper argued that the lower end of this range of permeabilities is more realistic in order to understand the behavior of the test sample we used in our measurements. It was also found that the estimated localized conductivities of the material particles are reasonably independent of the thicknesses of the electrical insulations between neighbouring particles.

On the other hand, the conductivities that are used in the literature, of the order of 10^7 S/m, were shown to be realistic [3–8]. This was done by characterizing the dependence between the scaling of the geometries and the estimated resistivity of the particles and showing that a resistivity of $10^{-7}\,\Omega$m corresponds to such scaling that is consistent with a microscope image of the SMC test sample. However, total uniqueness of the estimated parameter is not achieved. If there are uncertainties in the scaling of the geometry imitations, there will be discrepancies in the estimated conductivity, even if computed losses and effective permeabilities agree with the measurements. Furthermore, the estimated permeabilities of the material particles were found to be independent of the scaling of the geometry imitations.

Declaration of Competing Interest

The authors declare that they have no known competing financial interests or personal relationships that could have appeared to influence the work reported in this paper.

Acknowledgment

The foundation of Emil Aaltonen and the Academy of Finland (grant agreement No 307675) are acknowledged for financial support. J. Vesa thanks Saara Göös for reading the paper and commenting on the style. This project has received funding from the European Research Council (ERC) under the European Union's Horizon 2020 research and innovation programme (grant agreement No 848590).

Appendix A

This appendix supplements Section 4.1. In that section, the estimated values of the magnitude of the localized permeability of the material particles were visualized in Fig. 5. In this appendix, the estimated values of the angle of the localized permeability and the estimated values of the resistivity of the material particles are presented. The results can be found in Figs. 11 and 12, respectively. The black crosses, denoting 'accepted' results, have been selected according to the criterion $e_2 < 0.8$, described in Section 4.1. They correspond to the 'accepted' permeabilities, presented in Fig. 5.

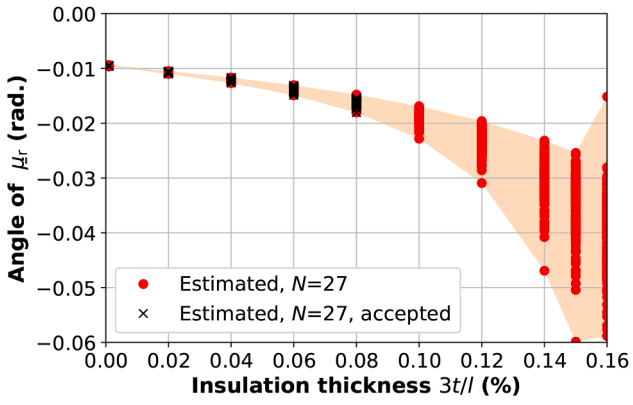

(a)

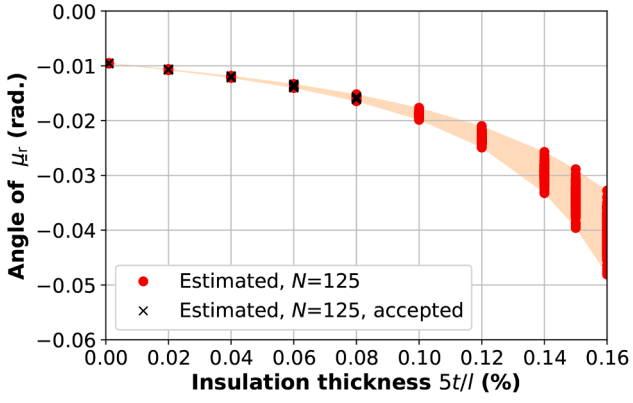

(b)

Fig. 11. Estimated angles of the localized permeability with respect to relative insulation thicknesses. (a) Estimations based on the 27-particle geometries. (b) Estimations based on the 125-particle geometries. The relative insulation thicknesses $3t/l$ and $5t/l$ have been explained in Section 4.1.

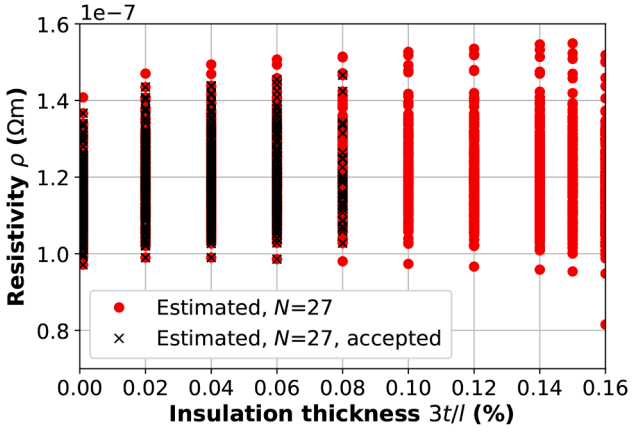

(a)

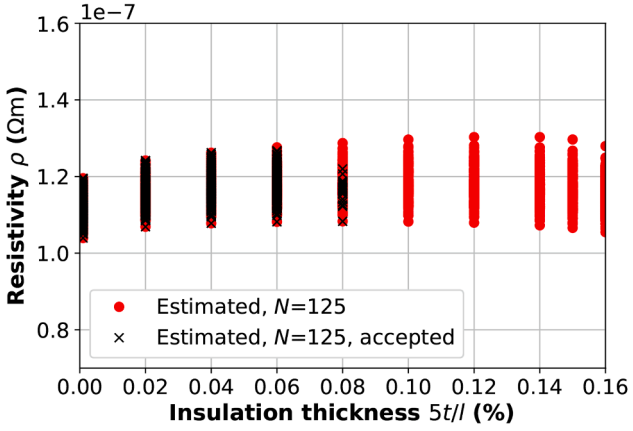

(b)

Fig. 12. Estimated resistivities with respect to relative insulation thicknesses. (a) Estimations based on the 27-particle geometries. (b) Estimations based on the 125-particle geometries. The relative insulation thicknesses $3t/l$ and $5t/l$ have been explained in Section 4.1.

Appendix B

This appendix supplements Section 4.2. In that section, the estimated values of the resistivity of the material particles were visualized in Fig. 9. In this appendix, the estimated values of the absolute value and the angle of the localized permeability are presented. The results can be found in Figs. 13 and 14, respectively. The results are independent of the scalings of the geometries.

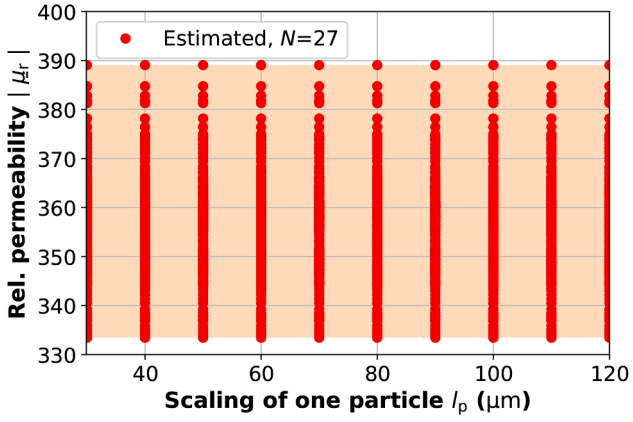

(a)

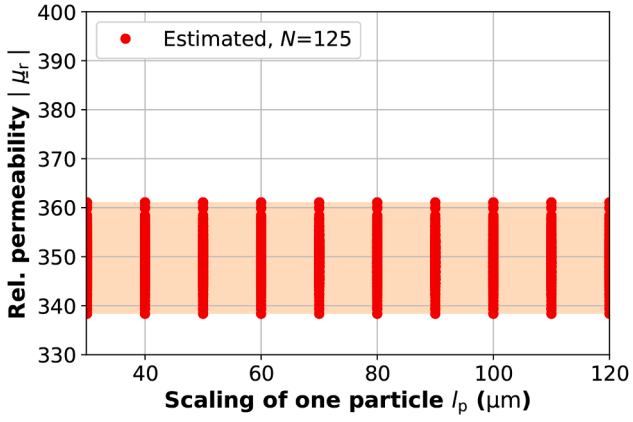

(b)

Fig. 13. Estimated absolute relative permeabilities with respect to the scaling of the material particles. (a) Estimations based on the 27-particle geometries. (b) Estimations based on the 125-particle geometries.

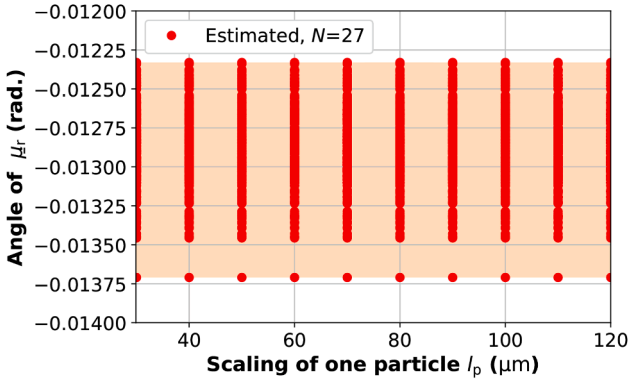

(a)

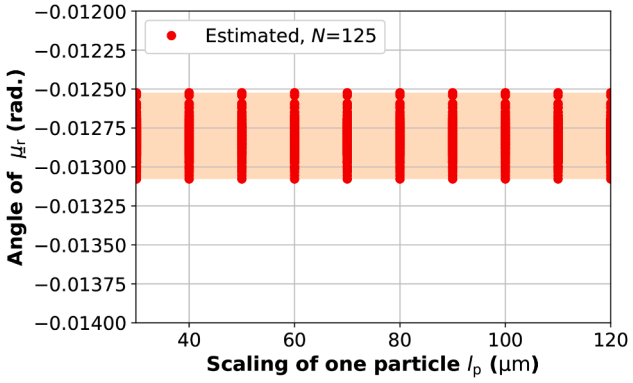

(b)

Fig. 14. Estimated angles of the localized permeability with respect to the scaling of the material particles. (a) Estimations based on the 27-particle geometries. (b) Estimations based on the 125-particle geometries.

References

[1] H. Shokrollahi, K. Janghorban, Soft magnetic composite materials (SMCs), J. Mater. Process. Technol. 189 (Feb. 2007).

[2] K. Sunday, M. Taheri, Soft magnetic composites: recent advancements in the technology, Metal Powder Report 72 (6) (Nov./Dec. 2017).

[3] A. Maruo, H. Igarashi, Analysis of magnetic properties of soft magnetic composite using discrete element method, IEEE Trans. Magn. 55 (6) (2019).

[4] X. Ren, R. Corcolle, L. Daniel, A 2D finite element study on the role of material properties on eddy current losses in soft magnetic composites, Eur. Phys. J. Appl. Phys. 73 (2016).

[5] X. Ren, R. Corcolle, L. Daniel, Losses approximation for soft magnetic composites based on a homogenized equivalent conductivity, Adv. Electromagn. 5 (2) (Sep. 2016).

[6] X. Ren, R. Corcolle, L. Daniel, A homogenization technique to calculate eddy current losses in soft magnetic composites using a complex magnetic permeability, IEEE Trans. Magn. 52 (12) (Dec. 2016).

[7] A. Bordianu, O. de la Barrière, O. Bottauscio, M. Chiampi, A. Manzin, A multiscale approach to predict classical losses in soft magnetic composites, IEEE Trans. Magn. 48 (4) (Apr. 2012).

[8] O. Bottauscio, V. Chiadò Piat, M. Chiampi, M. Codegone, A. Manzin, Nonlinear homogenization technique for saturable soft magnetic composites, IEEE Trans. Magn. 44 (11) (Nov 2008).

[9] T. Sato, S. Aya, H. Igarashi, M. Suzuki, Y. Iwasaki, K. Kawano, Loss computation of soft magnetic composite inductors based on interpolated scalar magnetic property, IEEE Trans. Magn. 51 (3) (Mar. 2015).

[10] Y. Ito, H. Igarashi, M. Suzuki, Y. Iwasaki, K. Kawano, Effect of magnetic contact on macroscopic permeability of soft magnetic composite, IEEE Trans. Magn. 52 (3) (Mar. 2016).

[11] J. Vesa, P. Rasilo, Producing 3-D imitations of soft magnetic composite material geometries, IEEE Trans. Magn. 55 (10) (Oct. 2019).

[12] Y. Ito, H. Igarashi, Computation of macroscopic electromagnetic properties of soft magnetic composite, IEEE Trans. Magn. 49 (5) (2013).

[13] H. Waki, H. Igarashi, T. Honma, Estimation of effective permeability of magnetic composite materials, IEEE Trans. Magn. 41 (5) (2005).

[14] T. Henneron, A. Benabou, S. Clénet, Nonlinear proper generalized decomposition method applied to the magnetic simulation of a SMC microstructure, IEEE Trans. Magn. 48 (11) (Nov. 2012).

[15] J. Vesa, P. Rasilo, Permeability Estimations of SMC Material Particles, IEEE Trans. Magn., Early Access 56 (9) (Jul. 2020).

[16] Magnetics Inc. C055106A2 datasheet, Revision Nov. 2016,https://www.mag-inc.com/Media/Magnetics/Datasheets/C055106A2.pdf.

[17] Scipy scipy.optimize.least_squares documentation, Cited in Jul. 2020,https://docs.scipy.org/doc/scipy/reference/generated/scipy.optimize.least_squares.html#scipy.optimize.least_squares.